International Journal of Fatigue 159 (2022) 106781

Contents lists available at ScienceDirect

International Journal of Fatigue

journal homepage: www.elsevier.com/locate/ijfatigue

Influence of induction hardening residual stresses on rolling contact fatigue lifetime

Maialen Areitioaurtena [a,*], Unai Segurajauregi [a], Martin Fisk [b,c], Mario J. Cabello [a], Eneko Ukar [d]

[a] Ikerlan Technology Research Centre, Basque Research and Technology Alliance (BRTA), Paseo J.M. Arizmendiarrieta 2, 20500 Arrasate-Mondragon, Spain
[b] Department of Materials Science and Applied Mathematics, Malmö University, Malmö, Sweden
[c] Division of Solid Mechanics, Lund University, P.O. Box 118, SE-221 00 Lund, Sweden
[d] Department of Mechanical Engineering, University of the Basque Country (UPV/EHU), Faculty of Engineering of Bilbao, Plaza Torres Quevedo 1, 48013 Bilbao, Spain

ARTICLE INFO

Keywords:
Life prediction
Multiaxial fatigue
Numerical modeling
Residual stresses
Rolling contact fatigue

ABSTRACT

Rolling contact fatigue is a unique mode of fatigue that components under cyclic contact loading experience. In this work, the impact of induction hardening residual stresses in rolling contact fatigue lifetime is investigated experimentally and numerically using the Dang Van multiaxial criterion. Various residual stress fields from induction hardening are simulated using the finite element method and are mapped into a classical mono-contact finite element model. The impact of induction hardened residual stresses on the lifetime of a component has been investigated, and the importance of incorporating the residual stress profile into fatigue life assessments is affirmed.

1. Introduction

In the early 1980s and 1990s many research institutes studied the relationship between heat treatments and structural integrity, concluding that the state of the material undoubtedly impacts on fatigue performance [1]. Rolling Contact Fatigue (RCF) is a unique mode of fatigue that components under cyclic contact loading experience. The alternating loading and unloading is produced by the movement of rolling elements, such as balls in a bearing raceway or wheels on a train rail. The movement, when combined with the pressure originated from the contact, creates a cyclic stress field in the subsurface area, which can fail by the initiation of a small crack that, due to damage accumulation, will propagate through the material until it reaches the surface. This effect occurs because the stress field in RCF, unlike in the common fatigue failure, typically follows the Hertzian mechanism, where the distribution of stresses forms a parabolic profile. Therefore, the maximum component of the stress is located slightly below the surface. RCF behavior is influenced by the hardness and the mechanical properties of the material. Thus, the surfaces of these components are typically hardened, either by thermochemical treatments (carburation, nitriding or carbonitriding) or by superficial heat treatments such as laser or induction hardening. These processes, however, introduce a residual stress profile in the surface region. Some studies have shown that surface hardened components exhibit greater RCF lifetime than through-hardened components [2]. RCF is a typical type of failure in bearing raceways [2–4], gears [1,5] and railways [6], among others. It is well established that, when a component of this type is properly installed, loaded and lubricated, its microstructure determines the RCF behavior [1,2], where a subsurface nucleated fatigue crack is formed, which propagates to the surface and causes spalling. Another form of fatigue crack can generate under RCF, where surface cracks (pitting) can appear because of surface defects or roughness. However, subsurface crack initiation is most common in industrial components, which is usually driven by shear effects [4,7,8].

Many authors have investigated the impact of different material characteristics on RCF. Walvekar and Sadeghi [9] presented a work where the impact of the hardness on RCF was studied, concluding that the depth of the hardened case, which was carburized in their study, impacts on the RCF behavior and finding an optimum case depth for their case study. Wei et al. [1] also reported that increasing the maximum hardness at the surface benefits fatigue lifetime delaying crack initiation. In their study, the authors incorporated a mechanical property gradient in the damage accumulation-based elasto-plastic finite element model, showing that intergranular damage depends on shear stress and normal stresses favor damage zone enlargement. The impact of surface characteristics such as residual stresses and surface roughness on combined rolling contact and wear failure in gears was investigated by Zhang et al. [10] and Liu et al. [11], concluding that

* Corresponding author.
E-mail address: mareitioaurtena@ikerlan.es (M. Areitioaurtena).

https://doi.org/10.1016/j.ijfatigue.2022.106781
Received 26 October 2021; Received in revised form 24 January 2022; Accepted 31 January 2022
Available online 12 February 2022

the position of the failure initiation (surface or sub-surface) depends on surface roughness, and thus, on wear behavior.

Xie et al. [7] studied the relation between surface hardness and subsurface position of maximum hardness with RCF life, concluding that an increased surface hardness generally extends fatigue life, although the subsurface hardness at the maximum stress point is more critical. However, the authors did not study the existing residual stress profiles in their specimens, which might have affected the obtained conclusions. In the literature it is possible to observe that RCF tests usually have a large dispersion in the obtained number of cycles, such as in [7], since RCF is highly affected by microstructural characteristics, leading to great ranges of fatigue life [12].

Regarding the impact of residual stresses in RCF, Guo and Barkey [13] drew a very interesting conclusion in their work, stating that the distribution of process-induced residual stresses affects in the near-surface initiated fatigue (about 20 μm) and the crack morphology rather than on the subsurface originated RCF, mainly affecting on the crack propagation angle. However, their study was conducted on hard turning and grinding induced residual stresses, where the presence of the compressive residual stresses is limited to a very small depth (approximately 100 μm), which is uncommon for induction hardened components. In the work by Ekberg et al. [14] residual stresses have been ignored due to the added complexity for the study. In the work by Wang et al. [5] the effect of residual stresses on RCF was studied for a carburized gear, finding a bilinear relation between the magnitude of the tensile residual stresses with respect to RCF life, considering that the normal stress leads to contact fatigue damage according to the Fatemi–Socie criterion.

Shen et al. [15] studied the impact of residual stresses and retained austenite in RCF lifetime for carburized AISI 8620 specimens, concluding that a considerable lifetime extension can be achieved with compressive residual stresses when compared to non-stressed specimens. The authors studied crack initiation and propagation, concluding that the presence of residual stresses does not affect spall shape.

Under RCF, the materials experience microstructural alterations due to an accumulation of strain, which represent the degradation of the material until ultimate failure. These alterations typically become apparent as dark etching regions (DERs), light etching regions (LERs), white etching bands (WEBs), and white etching areas (WEAs) [2]. When observed under an optical microscope after Nital etching, DERs are revealed as regions that appear darker than the matrix structure and they generally appear in the later stage of RCF. The formation of DERs is thought to be influenced by the existing stresses and time under these, which cause a stress-induced tempering, in which ferrite zones begin to form, decreasing the hardness. Usually, the greater the stress and the longer the period, the higher DER density and the wider the area [2,8,16].

Life assessment of components under RCF is usually carried out with different multiaxial fatigue criteria that have been proposed in the literature. The fatigue criteria can be classified into two main types: criteria using critical plane approach and criteria not using the critical plane approach. Both of them have been widely accepted, but the Dang Van criterion remarkably stands out among others, especially for the case where residual stresses are present, as used in [14,17,18]. Dang Van does not use a critical plane approach, although the multiaxiality of the loading is considered by means of critical stress quantities.

To date, only a few studies have investigated the association between induction hardening and RCF. This study intends to determine the extent to which the induction hardening induced residual stress profile affects RCF performance. In the following, induction hardening residual stresses are calculated and accounted for a RCF numerical model. Life assessment under the Dang Van multiaxial damage criterion is carried out, where several stress quantities are evaluated. Experimental validation of the life assessment is also performed, observing the influence of the residual stresses into RCF lifetime.

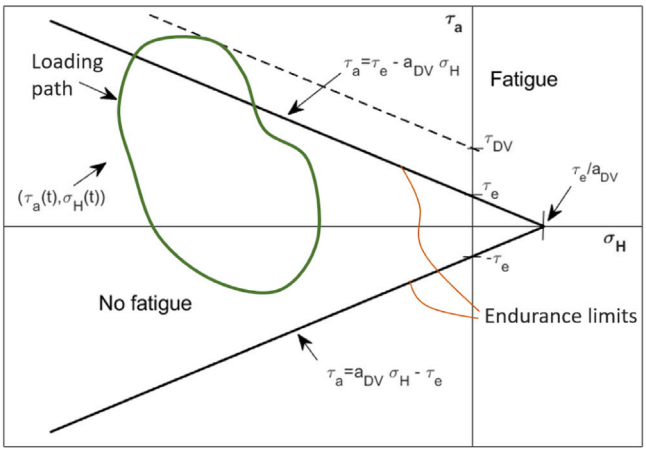

Fig. 1. Dang Van criterion under a random loading path (in green). (For interpretation of the references to color in this figure legend, the reader is referred to the web version of this article.)

2. Fatigue criteria for life assessment

Among the different multiaxial fatigue criteria that have been developed in the literature, in this work the Dang Van criterion is used, which is typically used in multiaxial stress states, particularly in the presence of residual stresses. Three different stress quantities are utilized and compared for the application of the Dang Van criterion in this work, which is presented in the following sections.

2.1. Dang Van fatigue criterion

The Dang Van criterion is a multiaxial high cycle fatigue criterion that considers the stresses in the meso and micro scales and is widely used for cases where residual stresses are present [14,19]. This criterion considers shear stresses as fatigue initiators and hydrostatic stresses that favor crack opening as main parameters. If either of these inequalities is fulfilled, it is assumed that fatigue initiation occurs. The Dang Ven critical stresses are

$$\tau_{DV1} = \tau_a(t) + a_{DV}\sigma_H(t) > \tau_e \tag{1}$$

$$\tau_{DV2} = \tau_a(t) - a_{DV}\sigma_H(t) < -\tau_e \tag{2}$$

where $\tau_a(t)$ is the time-dependent value of the shear stress at the most critical plane, $\sigma_H(t)$ is the hydrostatic stress at the material point, τ_e is a material parameter that represents the fatigue limit in pure shear and a_{DV} is a material parameter that represents the influence of hydrostatic stress. For more theoretical details on the calibration of the Dang Van criterion, the interested reader is referred to [19,20].

A graphical display of the Dang Van criterion is shown on Fig. 1 under a random loading path (in green). It is composed of two endurance limits (from Eqs. (1) and (2)) that determine if fatigue will occur. The enclosed area between the two limits defines the no fatigue zone, while any point of the loading path at the outer zone will suffer some fatigue damage.

The dashed tangent lines to the stress path determine the critical Dang Van stresses that are susceptible to damage (τ_{DV} in the figure) and these are used in a Wöhler diagram. Dang Van [20] postulated that the danger of fatigue failure is defined by

$$d = \max\left(\frac{\tau(t)}{\tau_e - a_{DV}\,\sigma_h(t)}\right) \tag{3}$$

where a value of $d > 1$ states that fatigue will occur according to the endurance limit proposed by Dang Van. The Dang Van criterion states that the most critical point on the loaded component is defined by

the combination of the hydrostatic stresses and shear stresses. Thus, one can use the potential damage Eq. (3) to evaluate the most critical crack nucleation point, which shall not necessarily coincide with the maximum shear stress point.

2.2. Critical stress quantities

Many authors have debated about the proper approach to establish the critical stress quantities that mostly affect RCF damage. The well-established Lundberg–Palmgren (LP) theory is based on the hypothesis that the maximum orthogonal shear stress in the subsurface describes the most critical stress factor for RCF damage and should be used in dynamic loading life assessments [21]. The LP theory is typically used in bearing life assessments in common engineering applications, as the selection process and rolling bearing calculations are determined by the ISO standard 281:2007 based on LP criterion [4,22]. The ISO standard recommends the use of the orthogonal shear criterion in order to estimate the damage, which does not require any critical plane examination [23]. Many authors have utilized the orthogonal shear criterion approach [18,24], as it is well established that RCF damage is mainly driven by shear stress. However, the LP theory does not account for hydrostatic stresses that favor crack closure. Thus, it has been stated that utilizing the orthogonal shear criterion without considering any other effect is the least conservative according to studies carried out by Lopez et al. [23] and Portugal et al. [22].

The shear stress quantity utilized for the Dang Van criterion is usually based on maximum shear stress, or Tresca stress, as originally stated by Dang Van et al. [19] but any other criteria can be used for the multiaxial stress state. Many other authors [7,25–27] determined that the octahedral shear stress is the most determinant quantity for RCF lifetime. Octahedral shear stress is related to invariant J_2 of the stress tensor and acts on octahedral planes generated in the direction of the principal stresses. Jalalahmadi and Sadeghi [26] determine that the depth of fatigue crack initiation is better described by the octahedral shear quantity, while Li et al. [27] state that considering octahedral shear stress as the failure-causing stress is more reasonable. The usage of the octahedral shear stress was suggested by Dang Van et al. [19] as an alternative to the Tresca stress, which is more commonly used in the literature [17,18].

Some authors that have compared several stress quantities conclude that the selection of the critical stress quantity becomes arbitrary under pure rolling condition in the elastic region [24] and that the selection of the damage criteria is not critical for finding damage location [3]. In this work, maximum shear stress (Tresca), orthogonal shear stress and octahedral shear stresses are used as the shear stress amplitude (τ_a) for the Dang Van multiaxial fatigue criterion where hydrostatic stresses are also considered, and the obtained results are compared. It is important to remark that, when using Tresca and octahedral shear stresses, all (τ, σ_H) components fall in the positive part of τ.

3. Experimental work

The experimental tests have been carried out in 42CrMo4 (AISI 4140) cylinders with a diameter of 20 mm and a length of 75 mm. This low alloy steel is commonly used for high resistance applications such as shafts, bearings or gears. The cylinders were manufactured from the core of a section of a large-size pitch bearing, where the microstructure is a soft ferrite and tempered martensite mixture with an approximate homogeneous hardness of 320 HV, which was measured using a Vickers microindenter. The chemical composition of the studied steel is shown in Table 1 in mass percentage. Optical Emission Spectrometry was used to measure the chemical constituents.

Table 1
Chemical composition of 42CrMo4 measured by Optical Emission Spectrometry. Data is given in mass percentage.

C	Mn	Cr	Mo	Si	P	S	F
0.45	0.90	1.2	0.3	0.40	0.025	0.035	Balance

3.1. Induction hardening experiments

Scanning induction hardening experiments have been carried out, where two residual stress levels have been generated. Specimens are named A and B. For both cases, the frequency was set to 17 kHz with a power of 38–45 kW and the inductor was a refrigerated single-turn coil with internal diameter of 27 mm. The scanning speed was set to 9 mm/s which resulted in a case depth of 4 mm for both sample types. The samples A were quenched using a 4% polymer concentration while the samples B were quenched with 12% polymer. The used polymer was AQUACOOL VSL-FF, which is a water dilutable polymer with an optimum operating temperature between 20 and 35 °C. This resulted in two residual stress profiles that were measured with the Incremental Hole Drilling technique. Type B rosettes were used to measure axial and hoop residual stresses for a depth of 1 mm following the non-uniform stress procedure in ASTM Standard E837-13a. Fig. 2 shows a photograph of the induction hardening process and a schematic representation of the process setup.

The hardness at the hardened case and core has been measured using a Vickers microhardness indenter with a 50 N force. Fig. 3 shows the experimentally measured hardness for both samples, where it is possible to observe that a fast cooling (sample A) provides higher hardness values in the transformed martensite, while a slower cooling rate (sample B) generates martensite of lower hardness. The depth of the hardened case is approximately 4 mm for both specimens. Although the power and scanning speed were kept constant in the experiments, it is expected that the slower cooling rate generates a slightly deeper hardened case because of the slower evacuation of the heat, which can be observed in the hardness measurements in Fig. 3. However, for the sake of simplicity, the problem has been simplified and it has been assumed that both samples have a hardened depth of 4 mm.

Because of the localized microstructural transformations that occur in the workpiece during induction hardening, it is not possible to obtain a specimen with a similar hardened case depth and hardness value and no residual stresses. Thus, we can only compare a non-stressed specimen theoretically and rolling contact fatigue experiments have only been carried out for samples A and B.

3.2. Rolling Contact Fatigue experiments

Authors such as Shen et al. [15], Guetard et al. [28] and Nygaard [29] studied the Rolling Contact Fatigue behavior by the three-ball-on-rod test. The test rig was presented by Glover [30] in 1981 and has been used ever since due to its simple set-up (see Fig. 4 a) for the evaluation of RCF in cylindrical components. The cylindrical test specimen is located in the center of the set-up and attached to the rotation system. Three balls are pressed radially against the surface of the test specimen by two standard tapered bearing cups. The loading system is constructed by trust bolts that are calibrated by compression springs, all of which are located at housing plates. Usually, the presented test is carried out in the elastic region (using contact pressures below 4000 MPa), some authors have worked on the plastic range in order to accelerate testing. Bhattacharyya et al. [2] performed tests at 5500 MPa contact pressure. Xie et al. [7] performed elastoplastic experiments to achieve failure between 10^6–10^7 cycles. However, no details were given about the contact pressure utilized in their study.

In the three-ball-on-rod Glover tester rotating motion is given to the 9.52 mm diameter test rig and the loading system (composed of three 12.7 mm balls, two tapered cups and the loading springs) is kept

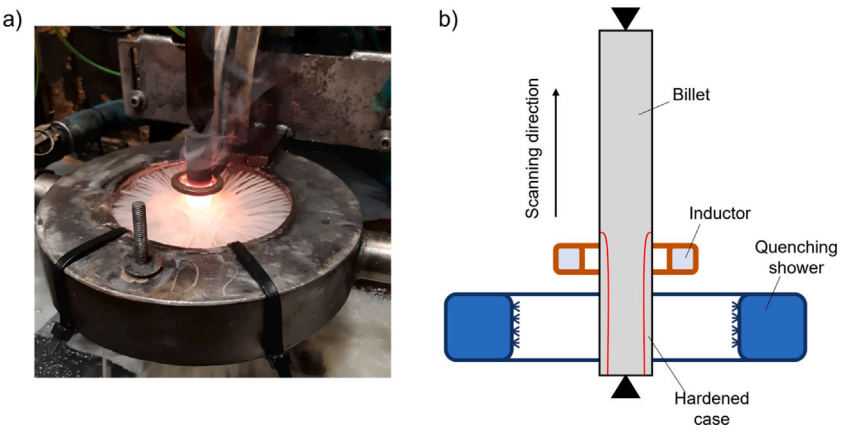

Fig. 2. (a) Induction hardening process and (b) schematic representation of the process setup.

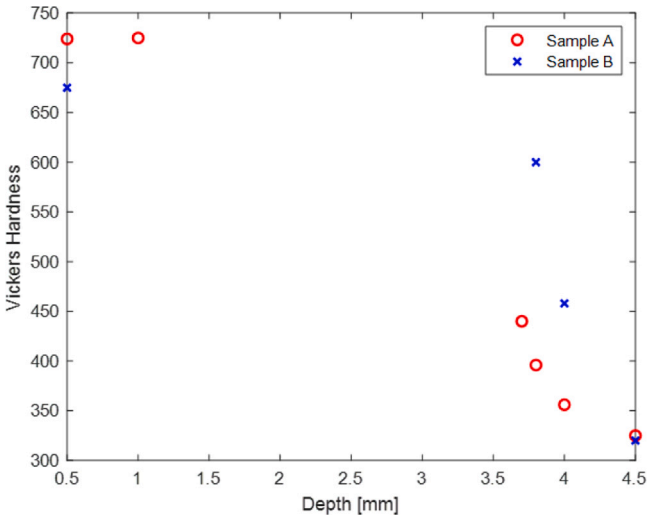

Fig. 3. Experimentally measured Vickers Hardness distribution for samples A and B.

static. For this work, the authors have modified the Glover tester to accommodate bigger test rigs in a previously developed test bench, which is suitable for testing medium-sized bearings. For that purpose, 20 mm diameter cylinders are placed statically at the center and the whole loading system is rotated at 400 rpm, where the 100Cr6 balls have a diameter of 36 mm. Fig. 4 shows a schematic representation of the modified three-ball-on-rod test (b) and a typical generated RCF crack morphology (c).

The tests were conducted at high contact pressures to accelerate failure. The balls were held by a 3D printed plastic retainer and six compression springs were used to apply the radial load. For each test, new balls and races were used, as the debris from the spalled material are retained within the system, causing significant plastic deformation points in the contact surfaces. The system was lubricated with a commercial ENGINE 7 lubricant through a drip system directed to the test specimen at a rate of 20 drops per minute. The tests were monitored by an accelerometer, which captured the vibration amplitude of the specimen holder. An inductive sensor was placed to count each ball cycle and determine the total contact stress cycles for the tests. Three tests were carried out for each sample type.

Table 2 shows the experimentally obtained RCF cycles to failure. Samples B spalled at 4.1, 7.1 and 3.9×10^6 cycles at a contact pressure of 4300 MPa, while samples A did not suffer any spalling after 10×10^6 cycles and were considered runout. The probabilistic behavior of fatigue in general, and RCF in particular, can be observed in the

Table 2
Experimentally obtained number of cycles to RCF failure. Samples were A considered runout after 10×10^6 cycles. The residual stress value indicated for the samples is the approximate measured value between 0.3 and 1 mm deep.

Residual stress	Test 1	Test 2	Test 3
A (−800 MPa)	10×10^6 (runout)	10×10^6 (runout)	10×10^6 (runout)
B (−400 MPa)	4.1×10^6	7.1×10^6	3.9×10^6

dispersion of fatigue life obtained for samples B, as RCF life is highly affected by the probability of having a crack initiator (usually carbides or non-metallic inclusions) in the subsurface region of the specimens.

The experimental results show that a minimum lifetime extension between 40% and 156% can be achieved when compressive residual stresses are of higher magnitude. However, the obtained rolling contact fatigue lives are not only directly linked to the residual stress state present in the specimens but also to their hardness.

Fig. 5 shows post-mortem images of the studied specimens B. In (a) a typical RCF spall can be observed in the sample B, where a v-shaped spall initiation is followed by a larger spalled and plastified area, caused by the continuation of the test after the initial spall occurred. In (b) it is possible to observe the v-shaped spall initiation area in detail, where a great roughness can be observed in the spalled region, showing plastically deformed wave-like surfaces consistent with RCF damage found in the literature.

In Fig. 5(c) an optical micrograph is shown, where a crack initiated at an inclusion can be observed. The specimens were radially cut and the surfaces were prepared for microscopical observation using abrasive grit sizes 80, 600 y 1200 and final polishing using diamond suspension of 9, 3 and 1 μm. The samples were observed microscopically and several crack initiation points were found in a depth between 360 μm and 440 μm. These crack were initiated at inclusions, where butterfly-shaped cracks originate from the inclusion. During RCF, the subsurface initiated cracks grow in a preferential direction, usually parallel to the surface of the specimen, until they change the propagation direction and grow towards the surface. Once the surface is reached, a spall appears in the surface, which is visible in Figs. 5 (a,b). In the crack shown in Fig. 5(c), the crack nucleated at a depth of 440 μm. A detailed view of the crack growth is given in the Figure.

4. Numerical simulation and life assessment

The numerical life assessment procedure designed for this work can be seen in Fig. 6. In the flowchart, it is possible to observe that the procedure starts with an induction hardening FE calculation, where the residual stresses are obtained. Then, these stresses are mapped into a contact model developed to evaluate the contact between the specimen and the balls, considering the previously calculated residual

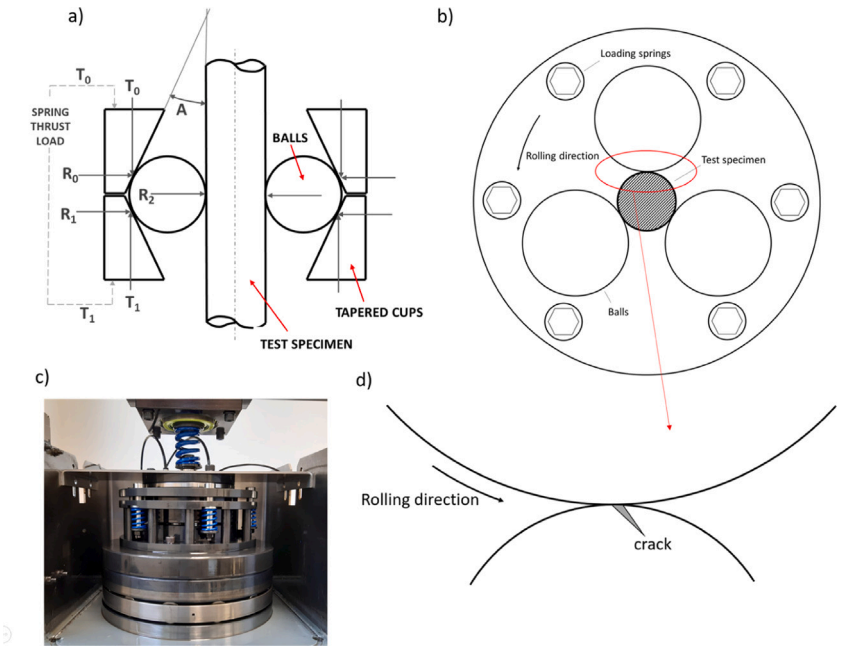

Fig. 4. Schematic representation of (a) three-ball-on-rod test developed by Glover [30], (b) top view and (c) photograph of the modified RCF tester and (d) a typically generated RCF crack morphology.

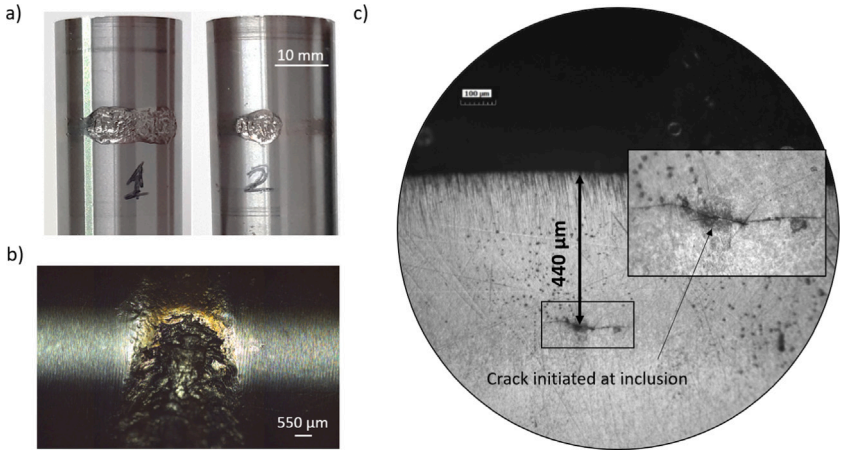

Fig. 5. (a) Shows RCF spalls and over-spalled region, (b) shows a closer look to the v-shaped spall initiation area and (c) shows an optical microscopy of a crack initiation at a depth of 440 µm.

stresses. For the life assessment section of the procedure, the results are transferred to Matlab, where the critical Dang Van stresses are calculated and plotted into the synthetic S-N curve in order to obtain the number of cycles before RCF failure for the studied component. Details of the different steps of the procedure are given in the following sections.

4.1. Modeling induction hardening

A numerical model has been used to compute the induction hardening process, where microstructure, hardness and residual stresses are computed. A semi-analytical approach has been used to solve the induction heating stage of the process. This modeling strategy is based on an initial finite element simulation, followed by analytical electromagnetic equations that are incorporated into a FE thermal solution to solve the coupled electromagnetic-thermal problem according to the procedure presented in [31]. The quenching stage has been simulated using a coupled multiphysical thermal–microstructural–mechanical model, where phase transformations and the generation of residual stresses are calculated.

In this work, a 3D FE model composed of 66k 8-noded hexahedral elements was used. The solution procedure uses a sparse matrix solver with implicit procedure and force-based convergence criteria. The computation time to solve the whole process, including the electromagnetic solution and the semi-analytical analysis used to model induction heating with a subsequent thermal–microstructural–mechanical coupled solution, took approximately 2 h.

Fig. 7 shows the numerically computed axial residual stresses in a transverse cross section of the sample A in (a) and B in (b). In (c) the mean value (normal distribution) and the standard deviation of the experimentally measured axial residual stress profile are shown for the two sample types, which are compared to the residual stresses computed numerically in the position indicated by the arrows. Three different specimens were measured for sample A and four for sample B in order to ensure repeatability of the induction hardening experiments and hole drilling measurements. In the figures, it is possible to observe that the residual stresses predicted by the simulation model are close

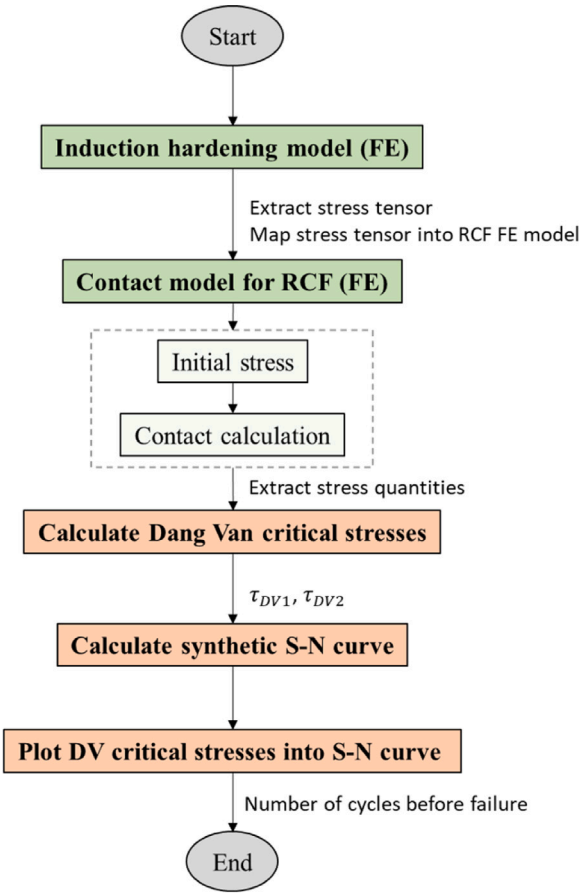

Fig. 6. Flowchart of the developed procedure for the numerical life assessment. Green boxes indicate FE modeling and orange boxes indicate Matlab calculations. (For interpretation of the references to color in this figure legend, the reader is referred to the web version of this article.)

to the span obtained in the experimentally measured residual stresses, especially in the region of interest where the RCF phenomenon occurs, between 0.3 mm and 0.6 mm.

Once the induction hardening residual stresses are obtained, the stresses are mapped into the rolling contact fatigue model, where the contact between the specimens and the balls is simulated. From the induction hardening model, the final stress tensor is extracted for each node. The stress tensor is mapped into the contact model by a triangulation weighting algorithm, where the values corresponding to the previous point coordinates are mapped into the corner nodes of the new mesh by scoping the closest nodes in the original mesh. In the contact model, two loading steps have been defined. The first step is used to incorporate the residual stresses into the contact model, where initial stresses are applied, and a static simulation is performed to achieve equilibrium without any external loads. On a second step, the contact with the ball is simulated by defining a fixed displacement to the ball so that the reaction forces equal the calculated ball-cylinder contact load.

4.2. Modeling of rolling contact fatigue

In order to compute the subsurface stresses, the contact analysis in homogeneous materials is usually carried out in elastic conditions following the Hertz stress distribution theory. However, in this work the contact sub-surface stress distribution has been evaluated using an mono-contact elastoplastic finite element model developed in ANSYS, as the plasticity level reached in the experimental tests cannot be neglected. All the simulations have been conducted in steady-state rolling condition and only 1/4 of the ball has been represented due to symmetry. The contact between the ball and the specimen has been considered frictional with a friction coefficient of 0.2 and has been modeled using contact elements with asymmetric behavior and augmented Lagrange formulation. The Coulomb friction model provided by ANSYS is used to model the contact between source and target faces. The contacting faces remain sticking with the applied load, with no sliding between them. Frictionless supports have been used to prevent the symmetry surfaces from moving freely.

Table 3
Summary of the material properties for 42CrMo4.

Property	Hardened case (724 HV5)	Hardened case (675 HV5)	Core (320 HV5)
Young's modulus (GPa)	205	205	205
Tangent modulus (GPa)	0.1 E	0.1 E	0.1 E
Poisons ratio	0.3	0.3	0.3
Yield strength (MPa)	1991	1850	830
Ultimate strength (MPa)	2595	2413	1091

Fig. 8 (a,b) shows the mesh used for the elasto-plastic model, composed of 1M nodes with a very fine mesh (mesh size is approximately 8×10^{-5} m) on the contact area. Quadratic elements were used for the model, where the areas outside the contact region were meshed using tetrahedral elements, while the area of interest was meshed with structured hexahedral elements.

To model the elastoplastic behavior of the material under high contact pressures, a plasticity model must be utilized. In this work, the elastoplastic behavior of the material has been considered using a bilinear isotropic hardening rule with von Mises yield criterion. The tangent modulus is considered to be 10% of Young's modulus. The yield strength is updated every time increment as

$$\sigma_Y = \sigma_{Y_0} + E_T \varepsilon_p \tag{4}$$

where E_T is the tangent modulus of the material and ε_p is the plastic strain.

For the FEM modeling, the hardness of the core has been considered 320 HV as measured in the as-received specimens and the hardness of the hardened case has been considered constant throughout the case with a value of 724 HV for samples A and 675 HV for samples B.

Vickers Hardness and mechanical properties have been correlated in a number of Refs. [32–34]. The correlation for Yield Strength and Ultimate Tensile Strength in MPa is given as

$$\sigma_Y = -90.7 + 2.876\,HV \tag{5}$$

$$\sigma_{UTS} = -99.8 + 3.723\,HV \tag{6}$$

Thus, to account for the different yield strength and ultimate tensile strength depending on the hardness of the steel, two regions have been differentiated in the model depending on their hardness. The region shaded in orange in Fig. 8 corresponds to the high hardness case, while the weaker material is established for the core. Table 3 shows a summary of the calculated material properties for the hardened case and core.

During rolling contact fatigue, the material experiences cyclic softening due to microstructural alterations caused by the solicitation. In the developed numerical model a steady-state rolling condition has been studied and this material behavior has not been considered.

The obtained numerical results for sample A, where the residual stresses have been considered as initial stress in the model, are shown on Fig. 9 for the contact region of the cylinder, where it is possible to observe (a) equivalent (von Mises) stress distribution under contact loading, (b) orthogonal shear stress, (c) Tresca stress and (d) octahedral shear stress. The contact pressure between the balls and the cylinder is 4300 MPa.

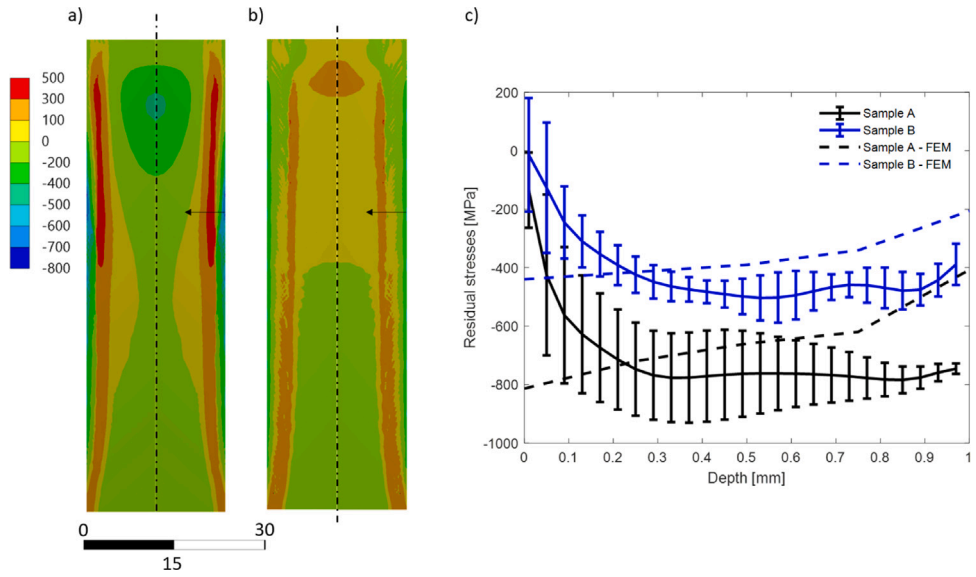

Fig. 7. Computed axial residual stresses in a transverse cross-section [MPa] for specimens A (a) and B (b), and (c) experimentally measured axial residual stresses by incremental hole drilling (mean values with standard deviation as error bars) compared to the residual stresses computed by FEM. The arrows indicate the position where residual stresses are measured.

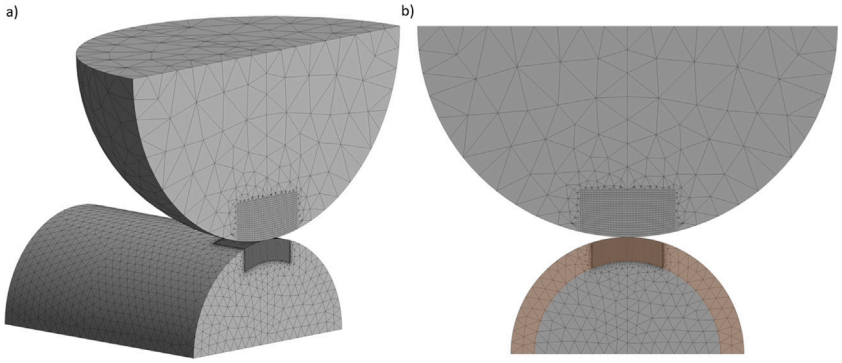

Fig. 8. Mesh used for the elastoplastic model. The hardened case has been colored in (b), representing the region where the mechanical properties differ from the core for both samples. (For interpretation of the references to color in this figure legend, the reader is referred to the web version of this article.)

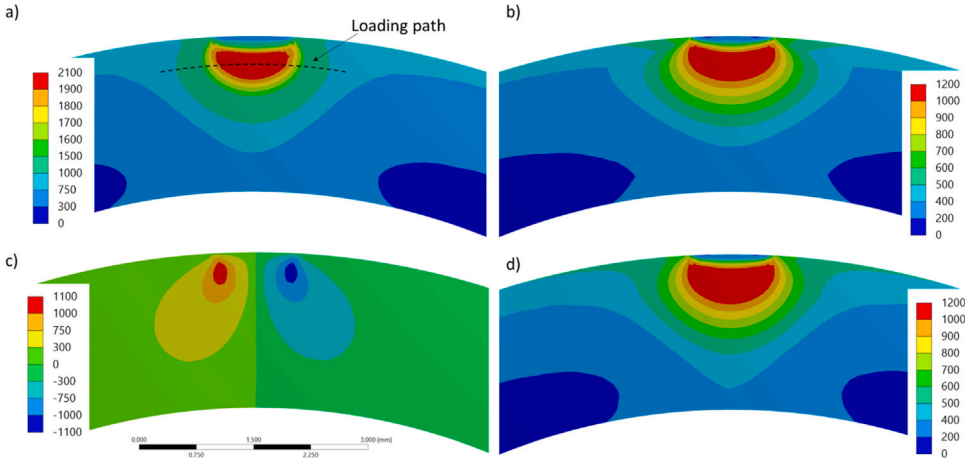

Fig. 9. Stress distributions [MPa] under contact loading: (a) equivalent (von Mises) stress, (b) Tresca stress, (c) orthogonal shear stress and (d) Octahedral shear stress. Loading path is marked in black dashed line.

4.3. Life assessment

Fig. 10 provides a typical load cycle computed with the elastoplastic model: von Mises, normal and shear stresses are shown, where the x axis denotes the position on the load path at one of the possible critical depths (see Fig. 9(a) for load path), where the 0 position is defined at the center of the contact, and the y axis denotes the stresses in MPa. In the figure it is possible to observe the multiaxiality on

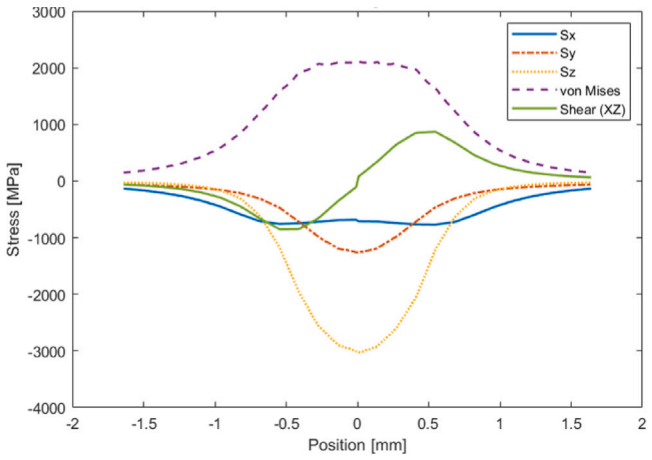

Fig. 10. Stress cycle showing von Mises, shear (XZ plane) and normal stresses in x, y and z directions for a non-stressed specimen.

RCF loading, where the variation on the normal stresses and the shear stress. A closer look to the multiaxial stress cycles shown in the figure, allows us to observe the complete reversal of the shear stress (thus, $R = -1$), showing the non-proportional stress distribution associated with the Hertzian contact, where it is possible to observe that the variation on the normal stresses and the shear stress does not follow any proportionality.

The Dang Van criterion is applied to the obtained numerical results, incorporating the three critical stress quantities as the critical shear stress τ_a for Eqs. (1) and (2). Material properties required for the application of the multiaxial criterion are evaluated based on the hardness of each sample. Since the stress quantities studied in this work provide different stress distributions in the sub-surface region, choosing a single critical stress path is not possible. Thus, in this work, we have studied the damage according to the Dang Van criterion for every node at the contact region instead of a single path. For each node, the three shear stress quantities and the hydrostatic stresses have been extracted from the FE results (extrapolated averaged nodal point values) and the (τ, σ_H) pairs have been plotted in the Dang Van diagram for the whole volume, see Fig. 11. Accordingly, the critical Dang Van stresses have been computed for each stress quantity. A graphical representation of the obtained results on the Dang Van multiaxial fatigue diagram is given in Fig. 11, where it is possible to observe the extracted (τ, σ_H) pairs according to the stress quantities. For each sample and shear stress quantity, the farthest point outside the endurance limits defined by the Dang Van criterion is found and a tangent line is drawn to calculate the critical Dang Van stress according to Eq. (1). For each case, the critical Dang Van stress is shown in the graph.

In the critical Dang Van results shown in Fig. 11 it is possible to observe that octahedral shear quantity gives higher critical stresses for the three specimens, while orthogonal shear provides the lowest critical Dang Van stresses for all sample types. The differences between the most and least conservative quantity are higher as the magnitude of residual stresses and the hardness increase.

4.4. Synthetic Wöhler curves

One of the reference standards for the design of rolling bearings is the procedure by Germanischer Lloyd [35], also known as GL guideline, which allows us to compute synthetic S-N (Wöhler) curves. For the case of non-welded forged and rolled parts the procedure takes into account the influence of several geometrical and material parameters. For this work, the following have been considered

- Surface roughness has been measured with a mean value of $R_z = 3.63\,\mu m$, as the specimens are grinded prior to testing.
- Notch factor has been set to 1 because we are applying the structural stress approach. Notch sensitivity has not been considered.
- Technology factor has been set to 1 as the thickness of the specimen is $<100\,mm$.
- Thickness effects have been ignored.
- Fatigue limit has been computed from the normative yield strength and updated considering the total influencing factor.
- A standard partial safety factor of 1.1 has been considered.
- Survival probability has been set to 50%.

Once all the effects have been considered, the slopes m_1 and m_2 of the S-N curve have been calculated, as well as the number of cycles and stress amplitudes at the upper fatigue limit (N_1 and σ_1, respectively) and knee (N_D and σ_A). The transformation of the computed uniaxial S-N curve to a shear stress S-N curve can be performed by dividing the result by $\sqrt{3}$ [36]. Fig. 12 shows the computed synthetic uniaxial S-N curves (solid lines) and the shear stress S-N curves (dashed lines) for both hardness values. The parameters calculated using the GL procedure are indicated in the figure.

The reader is referred to Appendix for further information on the influencing parameters and computation procedure.

5. Results and discussion

In Fig. 13 an optical micrograph of a sample A is shown, where a dark etching region is found in a non-spalled specimen after 10×10^6 cycles, which indicates that RCF failure should occur after a reduced number of cycles, as DERs are associated to the latest stage of RCF prior to complete failure. The size of the DER found in the non-spalled specimens is approximately 1 mm wide, 0.4 mm deep and begins at a distance of 0.1 mm from the surface, which is in correlation with DERs found in the literature. The dimensions of the DER found in the non-spalled specimens is compared to the numerically obtained plastic strain in the superimposed figure, where it is possible to observe that the size and pattern of the DER can be properly identified in the numerical model as the region where plastic deformation is reached.

In the following sections the influence of residual stresses on rolling contact fatigue lifetime and critical damage values and location is discussed.

5.1. Comparison of critical stress quantities based on life assessment

In Fig. 14 the numerical and experimental results are plotted in the synthetic S-N curves. The stresses shown in the figures are the critical Dang Van shear stresses computed from the three stress quantities studied in this work, shown in Fig. 11. Four types of specimens are shown in the figures: samples A and B and non-stressed theoretical samples with hardness values corresponding to samples A and B. For specimens A and B where experimental results exist (shown in Table 2), the obtained number of cycles are plotted into the S-N curves. Since it is impossible to measure the experimentally applied stress, numerically calculated stresses are used to complete the experimental (τ, N) couples in the S-N curves. For the four types of specimens, the presented numerical procedure has been used to calculate the stresses and the synthetic S-N curves have been used to calculate the theoretical number of cycles to failure. Thus, Fig. 14 shows the difference between theoretically and experimentally obtained number of cycles to failure for samples A and B, where it is possible to observe that the samples with higher compressive stresses and hardness values (samples A) can generally sustain a larger number of cycles under RCF than lower stressed specimens. This behavior have been validated with the performed experimental tests.

The predictions obtained for samples B using Tresca stress and octahedral stress as recommended by Dang Van et al. [19] appear to be too conservative, as failure would theoretically be expected earlier than experimentally obtained results, especially in the case of the octahedral shear, where the error in the prediction is the greatest. On the other

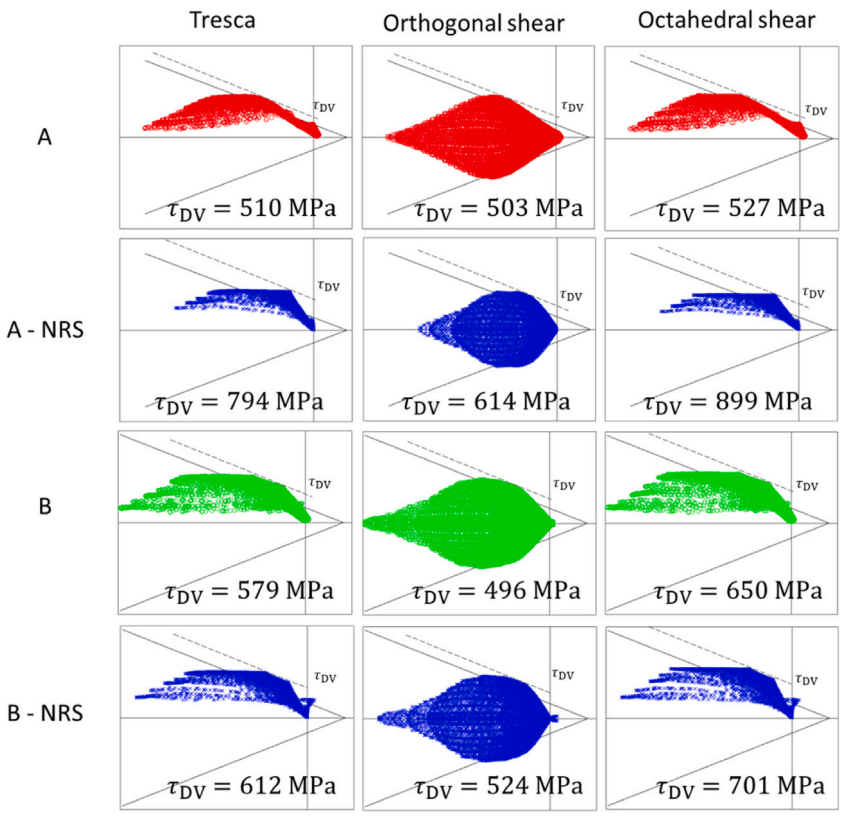

Fig. 11. Dang Van diagram with loads on selected volume. Rows refer to sample A (1), sample A without residual stresses (2), sample B (3), sample B without residual stresses (4). Columns refer to Tresca (1), orthogonal shear (2) and octahedral shear (3).

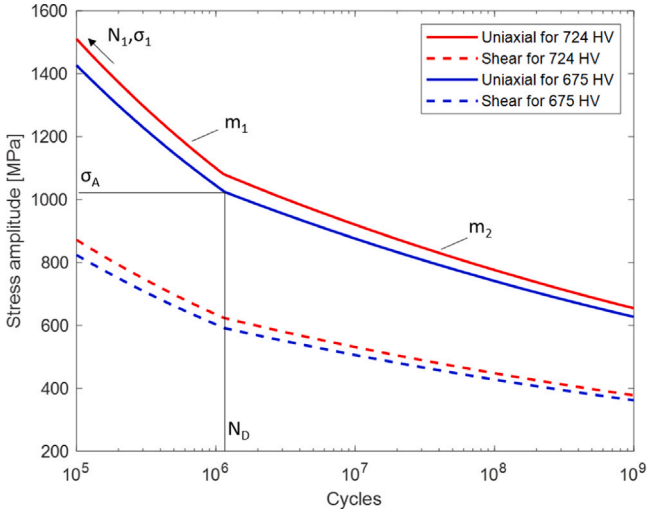

Fig. 12. Calculated synthetic S-N curves for uniaxial (solid line) and shear (dashed line) stresses for two different hardness values, calculated using the GL procedure.

hand, the results provided using the orthogonal quantity overestimate the obtained life, where the prediction states that failure would be expected at 12.9×10^6 cycles. For these samples, the lifetime difference between the specimen with and without residual stresses is between 245×10^3 and 6.8×10^6 cycles depending on the used stress quantity.

For the unspalled samples A, the three shear stress quantities provide similar results. The three critical shear stress quantities predict failures between 10.9×10^6 and 20×10^6 cycles. Although failure has not been reached in specimens A after 10×10^6 cycles, the DER found in the non-spalled specimens might indicate that RCF failure could occur in a short number of cycles, as DERs are associated to the latest stages of RCF. When it comes to the comparison between the specimens with and without residual stresses, considering residual stresses for specimens with a high hardness value such as in samples A is highly recommended as the lifetime difference between the theoretical samples is between 10.8×10^6 and 18.6×10^6 cycles depending on the used stress quantity.

Table 4
Summary of theoretical and experimental number of cycles to failure according to the three stress quantities. ND indicates that no data is available. NRS indicates the sample with no residual stresses.

	Theoretical (FE-based)			Experimental
	Tresca	Orthogonal	Octahedral	
A	17×10^6	20×10^6	10.9×10^6	10×10^6 (runout)
A-NRS	187×10^3	1.4×10^6	79×10^3	ND
B	1.5×10^6	12.9×10^6	574×10^3	$3.9 - 7.1 \times 10^6$
B-NRS	887×10^3	6.1×10^6	329×10^3	ND

5.2. Impact of residual stresses on life assessment

In Table 4 the numerically obtained RCF lives are summarized and compared with the experimental number of cycles to failure.

In summary, when the hardness is kept constant, it is possible to find a big difference between the predicted lifetime for the stressed and non-stressed samples, especially for the case where high compressive residual stresses are present.

As an example, according to the Tresca stress quantity with the Dang Van multiaxial criteria in specimen A, a specimen for which residual stresses have not been considered in the simulations would spall at 187×10^3 cycles while a specimen with high compressive residual stresses considered in the FE model would exhibit a much longer lifetime (17×10^6 cycles). The difference between stressed and

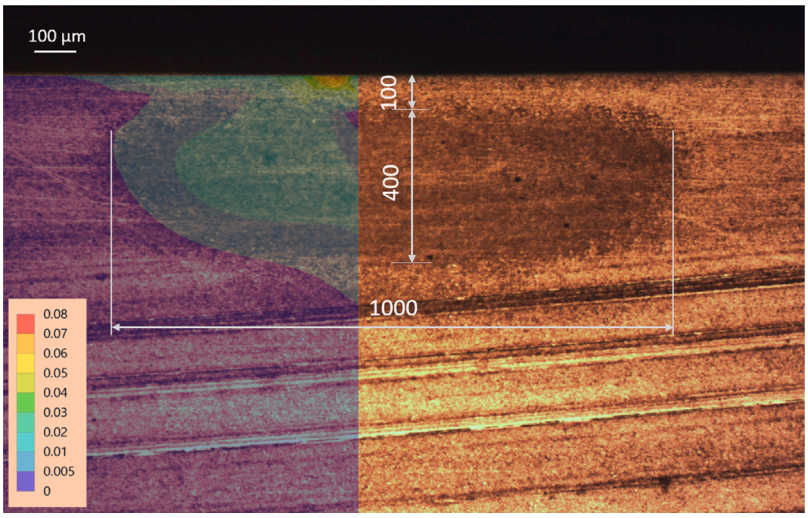

Fig. 13. Optical microscopy sample of a non-spalled specimen (x50 magnification) and a superimposed FE plastic strain. Dark etching region is approximately 1 mm wide, 0.4 mm deep and begins at a 0.1 mm distance from the surface.

Table 5
Summary of the maximum damage values and critical damage depths (in mm) according to the three critical shear stress quantities.

	Tresca		Orthogonal		Octahedral	
	Damage	Depth	Damage	Depth	Damage	Depth
A	1.2	0.39	1.2	0.39	1.2	0.39
A-NRS	1.77	0.78	1.42	0.44	1.94	0.78
B	1.47	0.97	1.27	0.53	1.61	0.97
B-NRS	1.54	1.02	1.34	0.53	1.7	1.02

non-stressed specimens can be observed for the three stress quantities studied in this work, becoming more evident as the residual stresses are more compressive and the hardness is increased. The highest difference can be observed for the Tresca criterion, while the results provided by the orthogonal shear quantity do not show such big differences. Therefore, it is possible to conclude that considering residual stresses in the fatigue life assessments greatly impacts lifetime prediction, as the predicted lifetime without considering the residual stress profile of the specimens would be much lower.

Thus, considering process-induced residual stresses in RCF analyses becomes of great importance, especially if the compressive residual stresses in the surface of the components has a large magnitude.

5.3. Critical damage location according to Dang Van

The Dang Van damage, computed with Eq. (3), gives the maximum damage that is found in the studied region, where one can observe if the most critical point of the component will suffer damage at some point of the loading cycles. The location of the most critical point and, thus, the most susceptible to crack nucleation, can be found when damage distribution is computed and displayed for the contact region. Fig. 15 shows damage distribution for samples A (a,b,c) and B (d,e,f). To obtain these distributions, the stress results have been extrapolated to the nodes from the integration points and Eq. (3) has been incorporated by user-defined expressions in ANSYS. The location of the most damaged point has been marked with a black cross for each figure. All points plotted in red have a damage value above 1.

Table 5 shows a summary of the maximum damage values and critical damage depths for all sample types.

In the case of sample A, the critical damage depth is 0.39 mm according to the three critical shear stress quantities, with a maximum damage value of 1.2. Damage distribution is shown on sample A in Fig. 15 for Tresca (a), orthogonal (b) and octahedral (c).

For sample B, the critical damage depth is 0.53 mm according to orthogonal shear and 0.97 mm for octahedral shear and Tresca. Damage distribution is shown on sample B in Fig. 15 for Tresca (d), orthogonal (e) and octahedral (f). When maximum damage values are observed, octahedral shear estimates greater damage values (1.61) than Tresca and orthogonal shear quantities (1.47 and 1.27, respectively). In this case, orthogonal shear provides lower maximum damage values.

In the case of the samples without residual stresses, the critical depths are larger than for the stressed specimens. In the case of sample A, the depth of the maximum damage location is between 0.44 mm (orthogonal shear) and 0.78 mm (Tresca and octahedral shear). In the case of sample B, the damage location coincides with the stressed specimen according to orthogonal shear (0.53 mm) but is larger according to Tresca and octahedral shear (1.02 mm). The maximum damage values are also higher when the stresses are not considered. For sample A the values vary from 1.42 and 1.94, while sample B has lower values, from 1.34 to 1.7.

In the figures it is possible to observe that the damaged volume is greater for the octahedral shear stress quantity, while orthogonal shear provides a smaller volume. Damaged volume is highly linked to the probability of survival since fatigue is mainly affected by microstructural characteristics, especially by steel cleanliness. Damaged volume has been incorporated into bearing design methodologies, as Weibull distributions are typically applied to the damaged volume calculated according to the L-P theory. Generally speaking, the larger the damaged volume, the higher the probability of failure, as the probability of finding a crack initiator in the stressed volume is higher.

When the numerically obtained critical damage depth is compared to the experimentally found crack initiation depths for samples B (between 360 µm and 440 µm), it can be concluded that orthogonal shear provides a better damage location prediction, as both Tresca and octahedral shear predict a much deeper maximum damage point.

In summary, it is possible to conclude that compressive residual stresses generally improve the component's behavior towards RCF damage by achieving a smaller damaged volume with lower maximum damage values. As already discussed, the octahedral shear stress quantity predicts a greater failure of the components for both sample types and the difference between the stressed and the non-stressed specimens is smaller according to orthogonal shear.

6. Conclusions

A methodology to incorporate process-induced residual stresses into rolling contact fatigue FE analyses has been developed. The methodology has been used to numerically assess the impact of induction

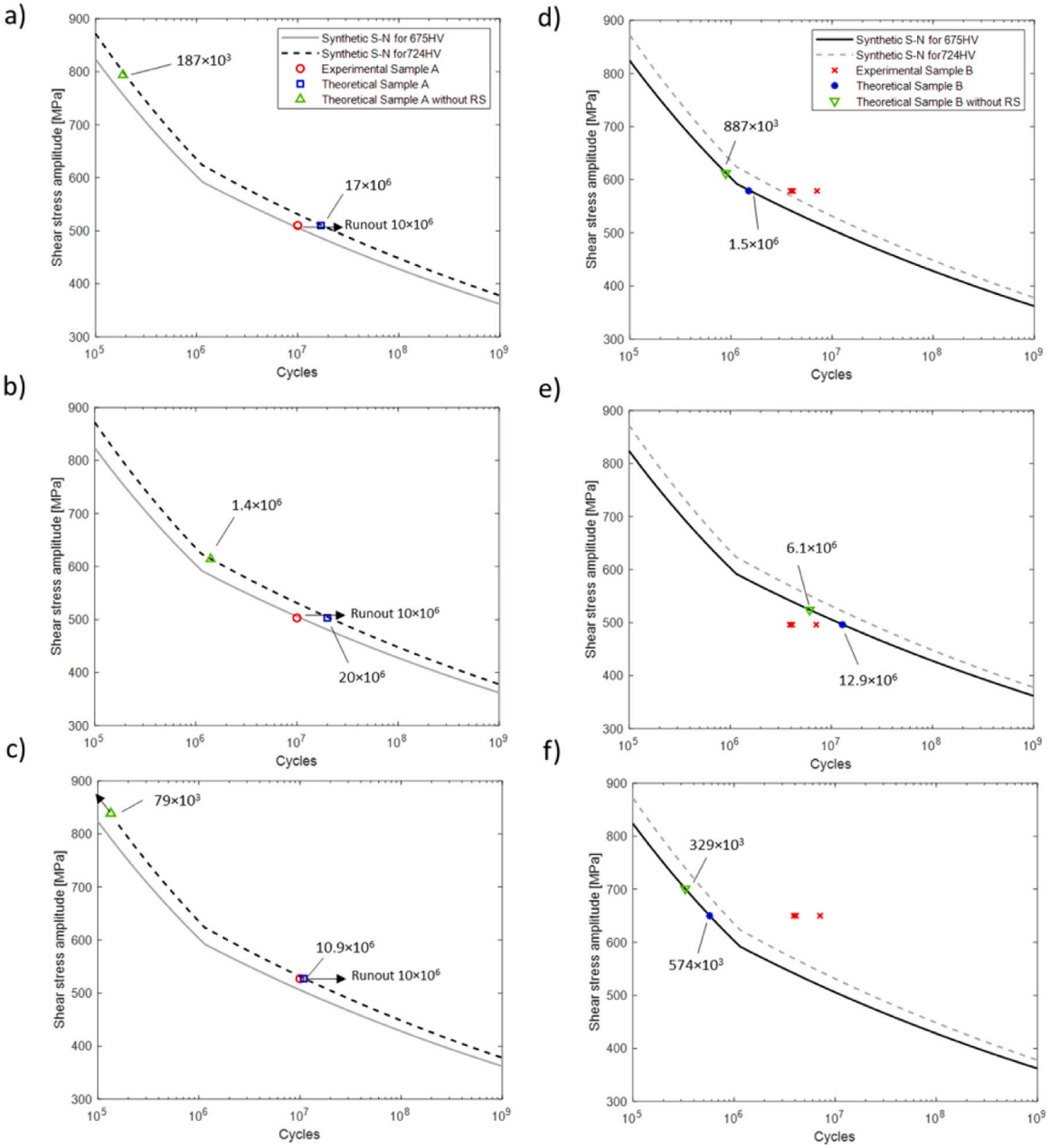

Fig. 14. Experimentally obtained and theoretical results shown on the computed S-N curves for samples A (left column) and B (right column), including theoretical samples without residual stresses. Dang Van equivalent shear stresses have been computed according to the three stress quantities: Tresca (a,d), orthogonal shear (b,e) and octahedral shear (c,f).

hardening residual stresses on rolling contact fatigue lifetime. For this purpose, three samples with different residual stress magnitudes have been compared by means of finite elements and synthetic S-N curves, concluding that, generally, the specimens with high compressive residual stresses can sustain a larger number of cycles before failure. The location of the most critical damage point has also been numerically studied with the developed methodology, concluding that larger residual stresses shift the damage initiation point towards the surface.

Experimental tests have been carried out in specimens with high (A) and low (B) magnitude residual stresses. The experimental results have shown that a minimum lifetime extension between 40% and 156% can be achieved in the case that the magnitude of the residual stresses is twice the magnitude of the low stress sample.

The multiaxial Dang Van criterion has been utilized for the analyses, where three different shear stress quantities have been considered as the critical shear stress required to apply the Dang Van criterion. The comparison between the numerically and experimentally obtained number of cycles to failure indicates that the Tresca quantity appears to be too conservative if used for failure-against-design analyses. The biggest difference between the studied stress quantities is found on the predicted location for crack nucleation, which indicates that octahedral shear provides more accurate results for samples B.

With the numerical and experimental studies carried out in this work, the importance of incorporating the residual stresses into numerical fatigue life assessments is affirmed. This work, therefore, demonstrates that compressive residual stresses improve the fatigue lifetime and that including the residual stress profiles into the fatigue life assessments improves the performed predictions. This fact is of high importance in industrial applications, as these components are typically greatly oversized in design-against-failure developments. This work also demonstrates that, when it comes to the application of induction hardening to components subjected to rolling contact fatigue, selecting

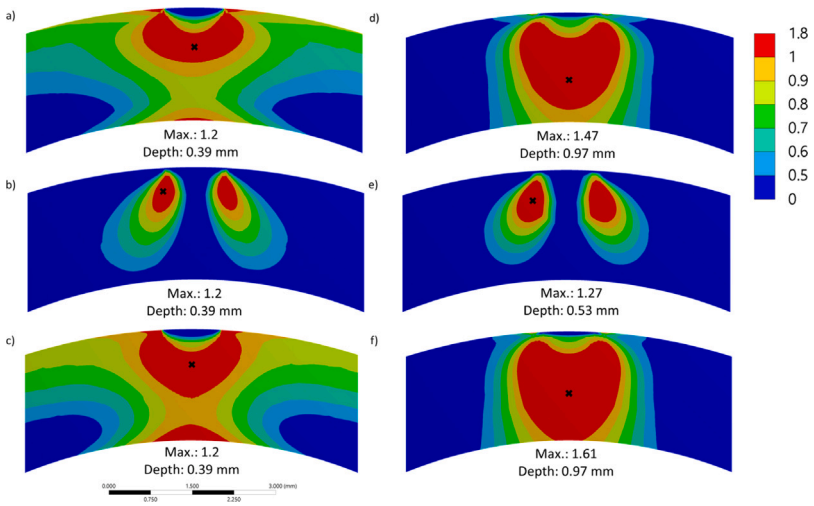

Fig. 15. Damage distribution in the sample A: (a) Tresca, (b) orthogonal shear stress and (c) octahedral shear stress and samples B: (d) Tresca, (e) orthogonal shear stress and (f) octahedral shear stress. Critical damage location has been marked with a black cross for each case. Maximum damage at the most critical location is shown for each case. All points plotted in red have a damage value above 1, meaning that endurance limit according to Dang Van has been exceeded. (For interpretation of the references to color in this figure legend, the reader is referred to the web version of this article.)

the right quenching medium can be critical for component performance, as the impact on the achieved hardness and residual stress profile is unquestionable.

Declaration of competing interest

The authors declare that they have no known competing financial interests or personal relationships that could have appeared to influence the work reported in this paper.

Acknowledgments

This project has received funding from the European Union's Horizon 2020 research and innovation program under grant agreement No 851245. The authors would also like to acknowledge the collaboration with TTT Goiko on the preparation of test specimens and post-mortem analyses.

Appendix. Procedure for the computation of synthetic S-N curves

The following procedure allows the calculation of synthetic S-N curves for non-welded forged and rolled parts [35].

1. The normative yield strength $\sigma_{0.2}$ and tensile strength σ_b are computed as

$$\sigma_{0.2} = 1.06\, R_{p0.2} \tag{A.1}$$

$$\sigma_b = 1.06\,\mathrm{Rm} \tag{A.2}$$

2. The fatigue strength for a polished specimen is given by

$$\sigma_W = 0.436\,\sigma_{0.2} + 77 \tag{A.3}$$

3. The mean stress sensitivity is computed as

$$\mathrm{M} = 0.00035\,\sigma_b - 0.1 \tag{A.4}$$

4. The total influencing factor is computed from a combination of various factors

$$F_{otk} = \sqrt{\beta_k^2 - 1 + \frac{1}{F_{ot}^2}} \tag{A.5}$$

where

- The technology factor depends on the thickness of the specimen. For $t \leq 100$ the technology factor is $F_t = 1$. For $t \geq 100$

$$F_t = \left(\left(2195 - \sigma_b\right)/1790\right) \tag{A.6}$$

- The surface roughness factor F_o is

$$F_o = 1 - 0.22\,\left(\log R_z\right)^{0.64} \cdot \left(\log \sigma_b\right) + 0.45\,\left(\log R_z\right)^{0.53} \tag{A.7}$$

- The combined surface and technology factor F_{ot} is

$$F_{ot} = 1 - \sqrt{\left(1 - F_o\right)^2 + \left(1 - F_t\right)^2} \tag{A.8}$$

- The notch factor β_k depends on the notch effect α_k and notch sensitivity n

$$\beta_k = \alpha_k / n \tag{A.9}$$

5. The fatigue strength of the component σ_{wk} can be computed as

$$\sigma_{wk} = \frac{\sigma_W}{F_{otk}} \tag{A.10}$$

6. The slopes of the S-N curve m_1 and m_2 are

$$m_1 = \frac{12.0}{F_{otk}^2} + 3 \tag{A.11}$$

$$m_2 = 2m_1 - 1 \tag{A.12}$$

7. The factor of influence of mean stress F_m is not applicable for the case of total reversal (where $R = -1$). Thus, its value is $F_m = 1$.
8. The stress amplitude at the knee of the S-N curve σ_A is computed as

$$\sigma_A = \sigma_{wk} \cdot F_m \tag{A.13}$$

9. The number of load cycles at the knee of the S-N curve is given by

$$ND = 10^{0.64 - \frac{2.5}{m_1}} \tag{A.14}$$

10. Several upgrading factors can be considered

- Survival probability S_{pu}. For 50% survival probability $S_{pu} = 1$ is considered while $S_{pu} = 2/3$ is used for a survival probability of 97.7%.

- Wall thickness dependent value S_t is computed as

$$S_t = \left(\frac{t}{25}\right)^{-0.1} \tag{A.15}$$

- Total upgrading factor is $S = S_{pu} \cdot S_t$

11. The partial safety factor of the material is usually assumed $\gamma_M = 1.1$.
12. The upgraded stress range at the knee of the S-N curve is given by

$$\Delta\sigma_A^* = 2\sigma_A \frac{S}{\gamma_M} \tag{A.16}$$

13. The upper limit of the fatigue life line is computed as

$$\Delta\sigma_1 = \sigma_{0.2} \frac{(1-R)}{\gamma_M} \tag{A.17}$$

14. The number of load cycles at the upper fatigue limit is calculated as

$$N_1 = N_D \left(\frac{\Delta\sigma_A^*}{\Delta\sigma_1}\right) \tag{A.18}$$

The reader is referred to Appendix 5.B.3.1 at Germanischer Lloyd [35] for further information on the influencing parameters.

References

[1] Wei P, Zhou H, Liu H, Zhu C, Wang W, Deng G. Modeling of contact fatigue damage behavior of a wind turbine carburized gear considering its mechanical properties and microstructure gradients. Int J Mech Sci 2019;156(November 2018):283–96.

[2] Bhattacharyya A, Londhe N, Arakere N, Subhash G. A new approach towards life prediction of case hardened bearing steels subjected to rolling contact fatigue. Mater Perform Charact 2017;6(4).

[3] Morales-Espejel GE, Gabelli A. The progression of surface rolling contact fatigue damage of rolling bearings with artificial dents. Tribol Trans 2015;58(3):418–31.

[4] Romanowicz PJ, Szybiński B. Fatigue life assessment of rolling bearings made from AISI 52100 bearing steel. Materials 2019;12(3):371.

[5] Wang W, Liu H, Zhu C, Du X, Tang J. Effect of the residual stress on contact fatigue of a wind turbine carburized gear with multiaxial fatigue criteria. Int J Mech Sci 2019;151(May 2018):263–73.

[6] Ekberg A, Kabo E, Andersson H. An engineering model for prediction of rolling contact fatigue of railway wheels. Fatigue Fract Eng Mater Struct 2002;25(10):899–909.

[7] Xie L, Palmer D, Otto F, Wang Z, Jane Wang Q. Effect of surface hardening technique and case depth on rolling contact fatigue behavior of alloy steels. Tribol Trans 2015;58(2):215–24.

[8] Zheng X, Zhang Y, Du S. The state-of-art of microstructural evolution of bearing materials under rolling contact fatigue. Mater Sci Technol 2019;1–19.

[9] Walvekar AA, Sadeghi F. Rolling contact fatigue of case carburized steels. Int J Fatigue 2017;95:264–81.

[10] Zhang B, Liu H, Zhu C, Ge Y. Simulation of the fatigue-wear coupling mechanism of an aviation gear. Friction 2021;9(6):1616–34.

[11] Liu H, Liu H, Zhu C, Tang J. Study on gear contact fatigue failure competition mechanism considering tooth wear evolution. Tribol Int 2020;147(November 2019):106277.

[12] Arakere NK. Gigacycle rolling contact fatigue of bearing steels: A review. Int J Fatigue 2016;93(June):238–49.

[13] Guo YB, Barkey ME. Modeling of rolling contact fatigue for hard machined components with process-induced residual stress. Int J Fatigue 2004;26(6):605–13.

[14] Ekberg A, Bjarnehed H, Lundbéan R. A fatigue life model for general rolling contact with application to wheel/rail damage. Fatigue Fract Eng Mater Struct 1995;18(10):1189–99.

[15] Shen Y, Moghadam SM, Sadeghi F, Paulson K, Trice RW. Effect of retained austenite - compressive residual stresses on rolling contact fatigue life of carburized AISI 8620 steel. Int J Fatigue 2015;75:135–44.

[16] Kang J. Mechanisms of microstructural damage during rolling contact fatigue of bearing steels (Ph.D. thesis), University of Cambridge; 2013, http://dx.doi.org/10.1023/B:QUAS.0000015546.20441.4a.

[17] Cheenady AA, Arakere NK, Londhe ND. Accounting for microstructure sensitivity and plasticity in life prediction of heavily loaded contacts under rolling contact fatigue. Fatigue Fract Eng Mater Struct 2020;43(3):539–49.

[18] Hoa Ngan N, Bocher P. Finite element analysis simulation of the effect of induction hardening on rolling contact fatigue. J Tribol 2018;140(6):061404.

[19] Dang Van K, Cailletaud G, Flavenot J, Le Douaron A, Lieurade H. Criterion for high cycle atigue failure under multiaxial loading. Biaxial Multiaxial Fatigue 1989;459–78.

[20] Dang Van K. Multiaxial fatigue criteria based on a multiscale approach. Academic Press; 2001, p. 457–63. http://dx.doi.org/10.1016/b978-012443341-0/50052-1.

[21] Lundberg G, Palmgren A. Dynamic capacity of rolling bearings. Stockholm: Generalstabens litografiska anstalts forlag; 1947.

[22] Portugal I, Olave M, Urresti I, Zurutuza A, López A, Muñiz Calvente M, Fernández-Canteli A. A comparative analysis of multiaxial fatigue models under random loading. Eng Struct 2019;182(November 2018):112–22.

[23] Lopez A, Zurutuza A, Olave M, Portugal I, Muniz-Calvente M, Fernandez-Canteli A. Pitch bearing lifetime prediction considering the effect of pitch control strategy. J Phys Conf Ser 2019;1222(1).

[24] Cheng W, Cheng HS. Semi-analytical modeling of crack initiation dominant contact fatigue life for roller bearings. J Tribol 1997;119(2):233–40.

[25] Harris TA, Yu WK. Lundberg-palmgren fatigue theory: Considerations of failure stress and stressed volume. J Tribol 1999;121(1):85–9.

[26] Jalalahmadi B, Sadeghi F. A voronoi finite element study of fatigue life scatter in rolling contacts. J Tribol 2009;131(2):1–15.

[27] Li F, Hu W, Meng Q, Zhan Z, Shen F. A new damage-mechanics-based model for rolling contact fatigue analysis of cylindrical roller bearing. Tribol Int 2018;120:105–14.

[28] Guetard G, Toda-Caraballo I, Rivera-Díaz-Del-Castillo PE. Damage evolution around primary carbides under rolling contact fatigue in VIM-VAR M50. Int J Fatigue 2016;91:59–67.

[29] Nygaard JR. Understanding the behaviour of aircraft bearing steels under rolling contact loading (Thesis), 2015.

[30] Glover D. A ball-rod rolling contact fatigue tester. In: Hoo J, editor. Rolling contact fatigue testing of bearing steels. Phoenix, AZ: American Society for Testing and Materials; 1981, p. 107–24.

[31] Areitioaurtena M, Segurajauregi U, Akujarvi V, Fisk M, Urresti I, Ukar E. A semi-analytical coupled simulation approach for induction heating. Adv Model Simul Eng Sci 2021;Manuscript.

[32] Pavlina EJ, Van Tyne CJ. Correlation of yield strength and tensile strength with hardness for steels. J Mater Eng Perform 2008;17(6):888–93.

[33] Fujita M, Kuki K. An evaluation of mechanical properties with the hardness of building steel structural members for reuse by NDT. Metals 2016;6(10).

[34] Wang W, Liu H, Zhu C, Bocher P, Liu H, Sun Z. Evaluation of rolling contact fatigue of a carburized wind turbine gear considering the residual stress and hardness gradient. J Tribol 2018;140(6):061401.

[35] Germanischer Lloyd. Rules and guidelines IV industrial services: Guideline for the certification of wind turbines. 2010, p. 389.

[36] Gabelli A, Lai J, Lund T, Rydén K, Strandell I, Morales-Espejel GE. The fatigue limit of bearing steels - part II: Characterization for life rating standards. Int J Fatigue 2012;38:169–80.